

# Metallurgical Aspects Influencing the Resistance to Steam Oxidation and Fracture Toughness of Select Advanced Replacement Alloys for LWR Core Internals



Approved for public release.  
Distribution is unlimited.

Lizhen Tan  
Tianyi Chen  
Bruce A. Pint

September 7, 2018

## DOCUMENT AVAILABILITY

Reports produced after January 1, 1996, are generally available free via US Department of Energy (DOE) SciTech Connect.

**Website** [www.osti.gov](http://www.osti.gov)

Reports produced before January 1, 1996, may be purchased by members of the public from the following source:

National Technical Information Service  
5285 Port Royal Road  
Springfield, VA 22161  
**Telephone** 703-605-6000 (1-800-553-6847)  
**TDD** 703-487-4639  
**Fax** 703-605-6900  
**E-mail** [info@ntis.gov](mailto:info@ntis.gov)  
**Website** <http://classic.ntis.gov/>

Reports are available to DOE employees, DOE contractors, Energy Technology Data Exchange representatives, and International Nuclear Information System representatives from the following source:

Office of Scientific and Technical Information  
PO Box 62  
Oak Ridge, TN 37831  
**Telephone** 865-576-8401  
**Fax** 865-576-5728  
**E-mail** [reports@osti.gov](mailto:reports@osti.gov)  
**Website** <http://www.osti.gov/contact.html>

This report was prepared as an account of work sponsored by an agency of the United States Government. Neither the United States Government nor any agency thereof, nor any of their employees, makes any warranty, express or implied, or assumes any legal liability or responsibility for the accuracy, completeness, or usefulness of any information, apparatus, product, or process disclosed, or represents that its use would not infringe privately owned rights. Reference herein to any specific commercial product, process, or service by trade name, trademark, manufacturer, or otherwise, does not necessarily constitute or imply its endorsement, recommendation, or favoring by the United States Government or any agency thereof. The views and opinions of authors expressed herein do not necessarily state or reflect those of the United States Government or any agency thereof.

Light Water Reactor Sustainability (LWRS) Program  
M2LW-18OR0406023

**METALLURGICAL ASPECTS INFLUENCING THE RESISTANCE TO STEAM  
OXIDATION AND FRACTURE TOUGHNESS OF SELECT ADVANCED  
REPLACEMENT ALLOYS FOR LWR CORE INTERNALS**

Lizhen Tan, Tianyi Chen, Bruce A. Pint

Date Published: September 7, 2018

Prepared by  
OAK RIDGE NATIONAL LABORATORY  
Oak Ridge, TN 37831-6283  
managed by  
UT-BATTELLE, LLC  
for the  
US DEPARTMENT OF ENERGY  
under contract DE-AC05-00OR22725



# CONTENTS

CONTENTS.....	iii
LIST OF FIGURES.....	v
LIST OF TABLES.....	vii
ACKNOWLEDGMENTS.....	ix
ABSTRACT.....	1
1. INTRODUCTION.....	2
2. EXPERIMENTAL.....	4
3. STEAM CORROSION BEHAVIOR.....	5
3.1 MASS CHANGE.....	5
3.2 SEM AND EDS RESULTS.....	6
3.3 TEM AND EDS RESULTS.....	8
3.3.1 Alloy 690.....	8
3.3.2 Alloy 725.....	10
3.3.3 Alloy X-750.....	12
3.4 DISCUSSION.....	13
3.4.1 Computational Alloy Thermodynamics.....	13
3.4.2 Exfoliation of Oxide Scale.....	15
3.4.3 Metal Thickness Loss by the Steam Exposures.....	18
4. FRACTURE TOUGHNESS TESTED SAMPLES.....	20
5. SUMMARY.....	23
REFERENCES.....	24



## LIST OF FIGURES

Figure 1. Time-dependent mass change of alloys 690, 725, and X-750 samples exposed to steam at 600 (black), 650°C (red). Each symbol indicates a measurement per sample. The dashed lines are in polynomial functions indicating the average trend. Results of alloy 690 exposed to hydrogenated [10] and aerated [11,12] pressured (21 or 25 MPa) water and alloy X-750 exposed to simulated BWR environment [13,15] are included for comparisons.....	5
Figure 2. Cross-sectional SEIs of the oxide scales formed on alloys (a-b) 690, (c-d) 725, and (e-f) X-750 exposed at (a, c, e) 600 and (b, d, f) 650°C for 5,000 h.....	7
Figure 3. EDS line scan profiles across the scales on alloys (a) 690, (b) 725, and (c) X-750 exposed at 650°C for 5,000 h. ....	8
Figure 4. (a) Bright-field STEM image of the 600°C-5000h-exposed alloy 690 and its (b-d) selected area EDS maps and (e) SAED pattern and corresponding (e') dark-field TEM image.....	9
Figure 5. (a) Bright-field STEM image of the 650°C-5000h-exposed alloy 690 and its (b) selected area EDS map and (c-d) SAED patterns.....	10
Figure 6. (a) Bright-field STEM image of the 600°C-5000h-exposed alloy 725 and its (b-g) SAED patterns taken from the locations marked on (a), together with (h) SAED pattern from a grain far from the scale and its corresponding (i) dark-field TEM image.....	11
Figure 7. (a) Bright-field STEM image of the 650°C-5000h-exposed alloy 725 and its corresponding (b) HAADF image and (c) SAED pattern from the locations schematically shown in (a). ....	11
Figure 8. EDS spectra of (a) oxides and (b) alloy phases in alloy 725 exposed at 600 and 650°C for 5,000 h. ....	12
Figure 9. (a) Bright-field STEM image of 600C-5000h-exposed alloy X-750 and its corresponding (b) selected area EDS maps and (c) SAED pattern.....	12
Figure 10. (a) Bright-field TEM image of 650°C-5000h-exposed alloy X-750 and its corresponding (b) SAED pattern.....	13
Figure 11. Computational thermodynamics calculated oxygen-partial-pressure-dependent phase content for oxidation of 1 mole alloys (a) 690, (b) 725 and (c) X-750, together with the composition variation of $M_2O_3$ at 600°C.....	14
Figure 12. Relationship between mass change, scale thickness, and calculated oxide phase fraction in outer scale for alloys 690 (circles), 725 (triangles), X-750 (diamonds) exposed at (a) 600°C and (b) 650°C. The open and filled black symbols denote the thickness data obtained from SEM and TEM characterization, respectively.....	16
Figure 13. Temperature-dependent thermal expansion coefficients of oxide phases and matrix alloys 690, 725, and X-750.....	17
Figure 14. Tracer diffusion coefficients of Cr, Fe, and Ni in Ni [24].....	18
Figure 15. (a) Thickness of the initial metal ( $t_0$ ) and the metal ( $t_m$ ) and scale ( $t_s$ ) after steam exposures; (b) Estimated metal thickness loss ( $\Delta t$ ) of alloys 690, 725, and X-750 exposed at 600 and 650°C for 5,000 h.....	19
Figure 16. Photos of fracture toughness tested samples at room temperature and 300°C (or 250°C) for ferritic alloys Grade 92 (G92) and 14YWT and austenitic stainless steels 316L and 310.....	21
Figure 17. Photos of fracture toughness tested samples at room temperature and 300°C for Ni-base superalloys 690, 718A, 725, and X-750. ....	22



## LIST OF TABLES

Table 1. Composition (wt%) of alloys 690, 725, and X-750 .....	4
Table 2. Fabrication condition of alloys 690, 725, and X-750 .....	4
Table 3. TEM characterized oxide and alloys phases for alloys 690, 725, and X-750 exposed at 600 and 650°C for 5,000 h .....	15



## **ACKNOWLEDGMENTS**

This research was sponsored by the U.S. Department of Energy (DOE), Office of Nuclear Energy (NE), for the Light Water Reactor Sustainability (LWRS) Program Research and Development (R&D) effort. We gratefully acknowledge the programmatic support provided by Keith J. Leonard of ORNL, Lead of Materials Aging and Degradation R&D Pathway of the LWRS Program.

The authors are grateful to Raj Pathania (Electric Power Research Institute [EPRI]) and Larry Nelson (JLN Consulting) for their managing and coordinating the Advanced Radiation Resistant Materials (ARRM) program, Tom Geer and Tracie Lowe of ORNL for preparing the metallographic samples and Eric Manneschildt of ORNL for taking photos of the fracture toughness tested samples. Xiang Chen and Mikhail Sokolov of ORNL are also appreciated for reviewing this report.



## ABSTRACT

Life extension of the existing nuclear reactors imposes accumulated damages, such as higher fluences and longer period of corrosion, to structural materials, which would result in significant challenges to the traditional reactor materials such as type 304 and 316 stainless steels. Advanced alloys with superior radiation resistance will increase safety margins, design flexibility, and economics for not only the life extension of the existing fleet but also new builds with advanced reactor designs. The Electric Power Research Institute (EPRI) teamed up with Department of Energy (DOE) to initiate the Advanced Radiation Resistant Materials (ARRM) program, aiming to develop and test degradation resistant alloys from current commercial alloy specifications by 2021 to a new advanced alloy with superior degradation resistance in light water reactor (LWR)-relevant environments by 2024.

Corrosion resistance in water environment is one of the fundamental properties required for LWR core internal materials. High-temperature steam oxidation tests are not only an accelerated life testing method to uncover potential failure modes in a short period of time, but also an approach to evaluate materials' resistance to accidental scenarios. Coupons, prepared from fourteen candidate alloys that were selected under the ARRM program, were exposed to 1 bar full steam with ~10 part-per-billion oxygen content at 600 and 650°C for up to 5,000 h, which were weighed at 500-h intervals.

Ni-base superalloys are an important class of alloys for reactor applications. Alloys 690, 725, and X-750 were three of the selected Ni-base superalloys exposed to the steam tests. This report summarizes the metallurgical aspects, such as alloy thermodynamics and the nature of the oxides and the diffusivities of primary elements, and their effects on oxidation behavior of the three alloys.

In addition to monitoring mass change, microstructures of the 5000h-exposed samples of alloys 690, 725, and X-750 were characterized using scanning and transmission electron microscopy and energy dispersive x-ray spectroscopy. Together with thermodynamic calculations, the scale constitution and its exfoliation behavior were discussed. Based on experimental and theoretical values, a new model was proposed to quantitatively estimate the metal thickness loss of the alloys. Alloy X-750 was found to have the best resistance to steam oxidation with the least metal thickness loss ( $<1 \mu\text{m}$ ), which were slightly superior to alloy 690. Alloy 725 exhibited the worst resistance to steam oxidation with the greatest metal thickness loss, e.g.,  $\sim 2.5 \mu\text{m}$  at 650°C, which is nearly three times of the metal thickness losses of alloys 690 and X-750 at 650°C. The greatest metal thickness loss of alloy 725 might be attributable to its high Mo content.

Photos of the fracture toughness tested samples of eight alloys are presented, which will be correlated with their fracture toughness results and planned tensile test results to select representative alloy samples for detailed microstructural characterization to reveal their microstructure and properties relationships.

## 1. INTRODUCTION

Nuclear power currently provides a significant fraction of the United States' non-carbon emitting power generation. In future years, nuclear power must continue to generate a significant portion of the nation's electricity to meet the growing electricity demand, clean energy goals, and to ensure energy independence. New reactors will be an essential part of the expansion of nuclear power. However, given limits on new builds imposed by economics and industrial capacity, the extended service of the existing fleets will also be required.

Nuclear reactors present a very harsh environment for components service. Components within a reactor core must tolerate high temperatures, water, stress, vibration, and an intense neutron field. With the nominal irradiation temperature of  $\sim 290^{\circ}\text{C}$  in light water reactors (LWRs), actual component temperatures range from  $270^{\circ}\text{C}$  to  $370^{\circ}\text{C}$  depending on the relative position of the component within the reactor core and relative amounts of cooling and gamma heating. Degradation of materials in this environment can lead to reduced performance, and in some cases, sudden failure. Extending the service life of a reactor will increase the total neutron fluence to each component and may result in radiation-induced effects not yet observed in LWR conditions, although this form of degradation has been observed in fast reactor conditions. Increases in neutron fluence may exacerbate radiation-induced or -enhanced microstructural and property changes. Comprehensive reviews on radiation effects on the traditional structural materials of LWRs can be found in Ref. [1,2,3].

It is desirable to have advanced alloys that possess greater radiation resistance than the traditional reactor materials, while having satisfactory performance in other primary properties. The use of such advanced alloys in replacing the traditional reactor materials for the extension of the existing fleets and the building of new reactors will bring improved safety margins and economics. To identify and develop advanced radiation resistant materials, Electric Power Research Institute (EPRI) has partnered with Department of Energy (DOE) Light Water Reactor Sustainability (LWRS) Program to conduct an Advanced Radiation Resistant Materials (ARRM) program. The EPRI report of "Critical Issues Report and Roadmap for the Advanced Radiation-Resistant Materials Program" [4] reviewed the current commercial and advanced alloys that are applicable as core structural materials of LWRs and laid out a detailed research plan to meet the goal of the program.

Oxidation resistance is one of the primary properties required to be screened for reactor materials, together with other properties such as fracture toughness, radiation-hardening, and irradiation-assisted stress corrosion cracking resistance. The materials will be down-selected for neutron irradiation study and comprehensive post-irradiation examinations to understand key factors governing superior properties, from which advanced replacement alloys will be developed and recommended for applications in LWR core internals. This report primarily presents the analytical results of high-temperature steam oxidation behavior of select Ni-base superalloys 690, 725 and X-750.

Ni-base superalloys are one of the classes of alloys investigated in this program, which are an important class of alloys used in nuclear reactors because of their excellent strength and corrosion resistance in general. Alloys 690, 725 and X-750 are a few outstanding examples, which are expected to have increased reactor applications. Alloy 690, derived from alloy 625 by reducing Mo and increase Cr for improved stress corrosion cracking resistance [5], has potential to replace alloys 600 and 625 for broader reactor applications. Alloy 725, also derived from alloy 625 by adding strengthening elements such as Nb, Ti and Al to favor age-hardening by forming  $\gamma''\text{-Ni}_3(\text{Nb,Ti,Al})$  and  $\gamma'\text{-Ni}_3(\text{Ti,Al})$  [6], is attractive for turbine applications, but rarely used in reactor primary circuit yet. Alloy X-750 is a precipitation-hardenable alloy, derived from alloy 600 by adding Ti and Al to favor the formation of secondary phase  $\gamma'\text{-Ni}_3(\text{Ti,Al})$  [7], which has more than three decades of applications, e.g., spacer grids in reactor core and other high-strength uses [8], in light water reactors (LWRs).

Corrosion resistance is one of the primary properties required to be screened for reactor materials. There are a number of studies reporting the corrosion behavior of alloy 690 exposed to different water environments. For example, exposing alloy 690 to simulated pressurized water reactor primary water at 360°C resulted in discrete coarse  $\text{NiFe}_2\text{O}_4$  particles in the outer oxide layer (up to  $\sim 2.5 \mu\text{m}$ ) and a mixture of Cr-rich  $(\text{Fe,Cr,Ni})_3\text{O}_4$ ,  $\text{Cr}_2\text{O}_3$  and metal in the inner layer (up to  $\sim 0.3 \mu\text{m}$ ) [9]. Exposing alloy 690 to hydrogenated subcritical (360°C and 25 MPa) and supercritical (400°C and 25 MPa) water for up to 2,000 h did not result in a significant difference in the oxide scales, except for the observation of NiO in the outer layer, compared to that formed in the simulated primary water [10]. However, exposure of alloy 690 to aerated supercritical water (SCW) at 450–600°C with 8 part-per-million (ppm) oxygen led to more extensive oxidation with a Ni-rich outer layer including NiO,  $\text{NiFe}_2\text{O}_4$  and  $\text{Ni}(\text{OH})_2$  and a Cr-rich inner layer including  $\text{Cr}_2\text{O}_3$  and  $\text{NiCr}_2\text{O}_4$  [11,12]. Unlike alloy 690, reports about water or steam tests of alloy 725 at elevated temperatures are scant. Similarly, water or steam tests of alloy X-750 have not been reported. A recent example is alloy X-750 exposed in simulated boiling water reactor (BWR) environment at 286°C and 8 MPa for up to 840 h, resulting in a  $\text{NiFe}_2\text{O}_4$  outer layer, a mixture of Cr-rich oxide with metal, and an intermediate layer of Ti- and Ni-rich needles with NiO between the outer and inner layers [13]. This result is similar to alloy X-750 exposed to simulated high flow velocity BWR water conditions, except for the absence of Ti-rich oxides and the presence of  $\text{Fe}_2\text{O}_3$  at the outmost surface [14]. However, exposure to SCW for up to 1,000 h at 500°C and 25 MPa with 10 part-per-billion (ppb) oxygen simply led to the formation of a fine  $\text{NiCr}_2\text{O}_4$  layer underneath a coarse  $\text{NiFe}_2\text{O}_4$  layer on alloy X-750 [15].

To evaluate the corrosion resistance of alloys 690, 725, and X-750 for their potential use in advanced reactor concepts and life extension of LWRs, accelerated testing was conducted in this work by exposing the alloys to 1 bar steam (starting water conductivity of 0065  $\mu\text{S}/\text{cm}$ ) at 600 and 650°C for 5,000 h. Additionally, the photos of the fracture-toughness-tested samples were taken to provide one of references for future microstructural characterization of select alloys.

## 2. EXPERIMENTAL

Commercial heats of alloys 690, 725, and X-750 were procured with the reported compositions in weight percent (wt%) listed in Table 1. The heat numbers and specific heat treatments that were applied to the heats are presented in Table 2.

**Table 1. Vendor reported composition (wt%) of alloys 690, 725, and X-750**

Alloy	Fe	Cr	Ni	Mo	Al	Ti	Nb	Si	Mn	C	N
690	10.38	29.44	59.33	0.01	0.23	0.35	0.01	0.05	0.15	0.03	0.01
725	7.94	21.52	57.60	8.07	0.17	1.35	3.41	0.04	0.04	0.01	-
X-750	8.44	15.68	71.02	-	0.72	2.61	0.85	0.06	0.04	0.04	-

**Table 2. Fabrication condition of alloys 690, 725, and X-750**

Alloy	Heat number	Melting method <sup>a</sup>	Heat treatment <sup>b</sup>
690	NX7075HK	VIM + ESR	1038°C 2.7h + AC
725	416408	VIM + VAR	1038°C 2h + FC + 725°C 8h + 56°C/h cooling rate to 621°C 8h + AC
X-750	418365	VIM + ESR	1080°C 2h + 715°C 20h + AC

<sup>a</sup> VIM – vacuum induction melting; ESR – electroslag remelting; VAR – vacuum arc remelting

<sup>b</sup> FC – fan cool; AC – air cool

Coupons (19 × 10 × 1.5 mm) were cut from the procured alloys by electro-discharge machining and ground to a 600 grit SiC finish, followed by ultrasonic cleaning in acetone and methanol in sequence. The exposures were conducted in three-zone tube furnaces with an alumina reaction tube and stainless steel endcaps. The deionized water was deaerated, filtered and atomized without a carrier gas to generate 1 bar steam with ~10 ppb oxygen content. The oxygen content is comparable to the oxygen level in the primary water chemistry (≤10 ppb) of pressured water reactors and significantly lower than the normal water chemistry (200–400 ppb) of boiling water reactors [16]. Five coupons per alloy were evaluated at each temperature and held in an alumina boat. The coupons were slowly heated to the target temperatures over ~4 h under Ar gas to limit oxidation, held for 500 h each cycle at 600 or 650°C and then cooled in the same manner for a total of 10 cycles. Mass change was measured each cycle using a Mettler-Toledo model XP205 balance with an accuracy of ±0.04 mg or ±0.01 mg/cm<sup>2</sup>.

Microstructural characterization was conducted on the 5000-h exposed coupons by means of scanning electron microscopy (SEM), transmission electron microscopy (TEM: JEOL JEM-2100F at 200 kV), and energy dispersive X-ray spectroscopy (EDS). For cross-sections, the coupons were Cu-plated prior to sample cutting and metallographic polishing in an epoxy mount. Focused ion beam (FIB: FEI Versa 3D Dual-Beam) was used to prepare electron transparent lamellae from the intact part of the steam-exposed coupons for TEM characterization. Progressive final cleaning steps using a 5 to 2 kV ion beam were employed to minimized possible artifacts on the lamellae from FIB processing. Selected-area electron diffraction (SAED) was performed to help phase identification.

### 3. STEAM CORROSION BEHAVIOR

#### 3.1 MASS CHANGE

The time-dependent mass changes of the steam-exposed coupons of alloys 690, 725 and X-750 are shown in Figure 1, with the black and red open symbols denoting the 600 and 650°C results, respectively. The dashed lines are polynomial fitting to indicate the time-dependent trends. After small mass gains during the first 1,500 h of exposure at 600°C, alloy 690 and 725 specimens began to show mass loss with alloy 690 having the highest mass loss. The mass losses of alloys 690 and 725 at 600°C were not stabilized within the 5,000-h exposure. In contrast, alloy X-750 specimens showed negligible mass changes at 600°C. At 650°C, alloy 690 exhibited moderate mass gains, approximately saturated at  $\sim 0.1$  mg/cm<sup>2</sup>, while alloy 725 had the highest mass gains approximately saturated at  $\sim 0.25$  mg/cm<sup>2</sup>. Alloy X-750 specimens showed the lowest mass gains but the greatest scatter. The transition from general mass losses at 600°C to mass gains at 650°C may suggest a relatively constant source of mass loss such as evaporation combined with increasing scale growth at the higher temperature. Mass loss could also be associated with scale spallation, but spallation typically increases with temperature.

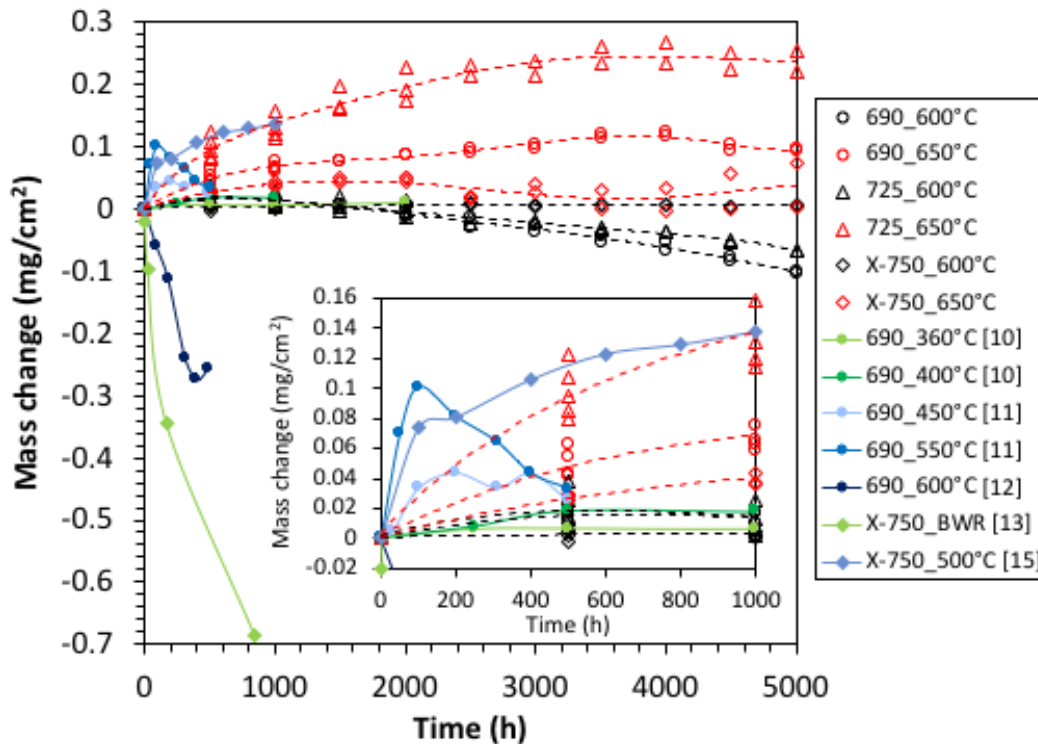


**Figure 1. Time-dependent mass change of alloys 690, 725, and X-750 samples exposed to steam at 600 (black), 650°C (red). Each symbol indicates a measurement per sample. The dashed lines are in polynomial functions indicating the average trend. Results of alloy 690 exposed to hydrogenated [10] and aerated [11,12] pressured (21 or 25 MPa) water and alloy X-750 exposed to simulated BWR environment [13,15] are included for comparisons.**

Literature mass change data for alloys 690 and X-750 exposed to different water environments are included in Figure 1 as filled symbols with solid lines for comparisons. The inset of Figure 1 shows the enlarged section to better reveal the mass changes within 1,000 h. Alloy 690 exposed to hydrogenated water

at 360°C (21 MPa) and 400°C (25 MPa) had minimal mass gains of nearly 0.01 and 0.02 mg/cm<sup>2</sup>, respectively [10]. The aerated water with 8 ppm dissolved oxygen under 25 MPa resulted in higher mass gains to up to 0.04 and 0.1 mg/cm<sup>2</sup> at 450 and 550°C, respectively [11]. However, such high mass gains were not retainable, which turned to have noticeable reductions in mass gains. The aerated water with 8 ppm oxygen at 600°C (25 MPa) resulted in noticeable mass losses [12]. The alloy 690 data under comparable pressures indicate that higher oxygen content and temperatures tended to result in greater instability to the mass changes from minor mass gains to noticeable mass losses. Temperature, oxygen content, and pressure as three primary test environment factors played a synergistic role in the corrosion behavior. Higher temperature and oxygen content would favor faster oxidation kinetics for thicker oxide scale formation, leading to mass gains followed by possible mass losses when the scales become too thick. Higher pressure would deteriorate scale integrity by forming pores in the scales that were observed on austenitic stainless steels [17,18], resulting in spallation of the scales and mass losses. The 600°C steam-exposed alloy 690 specimens in this work had significantly less mass loss than the alloy 690 specimens exposed in aerated water at 600°C, which might have been benefited from the lower oxygen content and pressure in the steam (~10 ppb and 1 atm) compared to that in the aerated water (8 ppm and 25 MPa). Additionally, the comparable mass change of alloy 690 between the exposures in steam at 600°C (this work) and in hydrogenated water at 360 and 400°C, which have a similar level of oxygen content, implies that temperature might not be a key factor governing mass change compared with oxygen content. Following the same trend with oxygen content as a key factor, alloy X-750 exposed in simulated BWR water at 286°C and 8 MPa had exceptional mass losses compared to the mass gains of alloy X-750 exposed in SCW at 500°C and 25 MPa with 10 ppb oxygen. However, the steam-exposed alloy X-750 in this work at 600 and 650°C exhibited noticeably lower mass gains than the SCW-exposed alloy X-750 at 500°C, considering their comparable oxygen content. The higher pressure in the SCW might have accelerated the oxidation rate.

### 3.2 SEM AND EDS RESULTS

The secondary electron images (SEIs) of the 5000-h-exposed samples in a cross-sectional view are shown in Figure 2. The images were taken at the same magnification with the oxide scale and deposited copper at the top of the images. The oxide scales are generally continuous. The scales on the 650°C-exposed samples primarily differ from the 600°C-exposed samples in three aspects: thicker scales; noticeable internal oxidation on alloy 690 (Figure 2b); thicker oxidation-influenced layer beneath the scales, which was up to 6, 12, and 2 μm for alloys 690, 725, and X-750, respectively, as indicated by the white double-arrows. The scale thickness follows the same descending order for the 600°C- and 650°C-exposed samples of alloys 725, 690, and X-750, except for minor difference for the 600°C-exposed samples with 0.67±0.19, 0.53±0.31, and 0.34±0.20 μm but noticeable difference for the 650°C-exposed samples with 2.13±0.27, 0.80±0.17, and 0.68±0.50 μm, respectively. The descending order for the 650°C-exposed alloys is consistent with the mass gain trend of the alloys as shown in Figure 1. Unlike alloys 690 and X-750, alloy 725 showed a dense lath-like phase in the oxidation-influenced layer beneath the scale. Additionally, some dark features appeared right beneath the scale on alloy 725 exposed at 650°C.

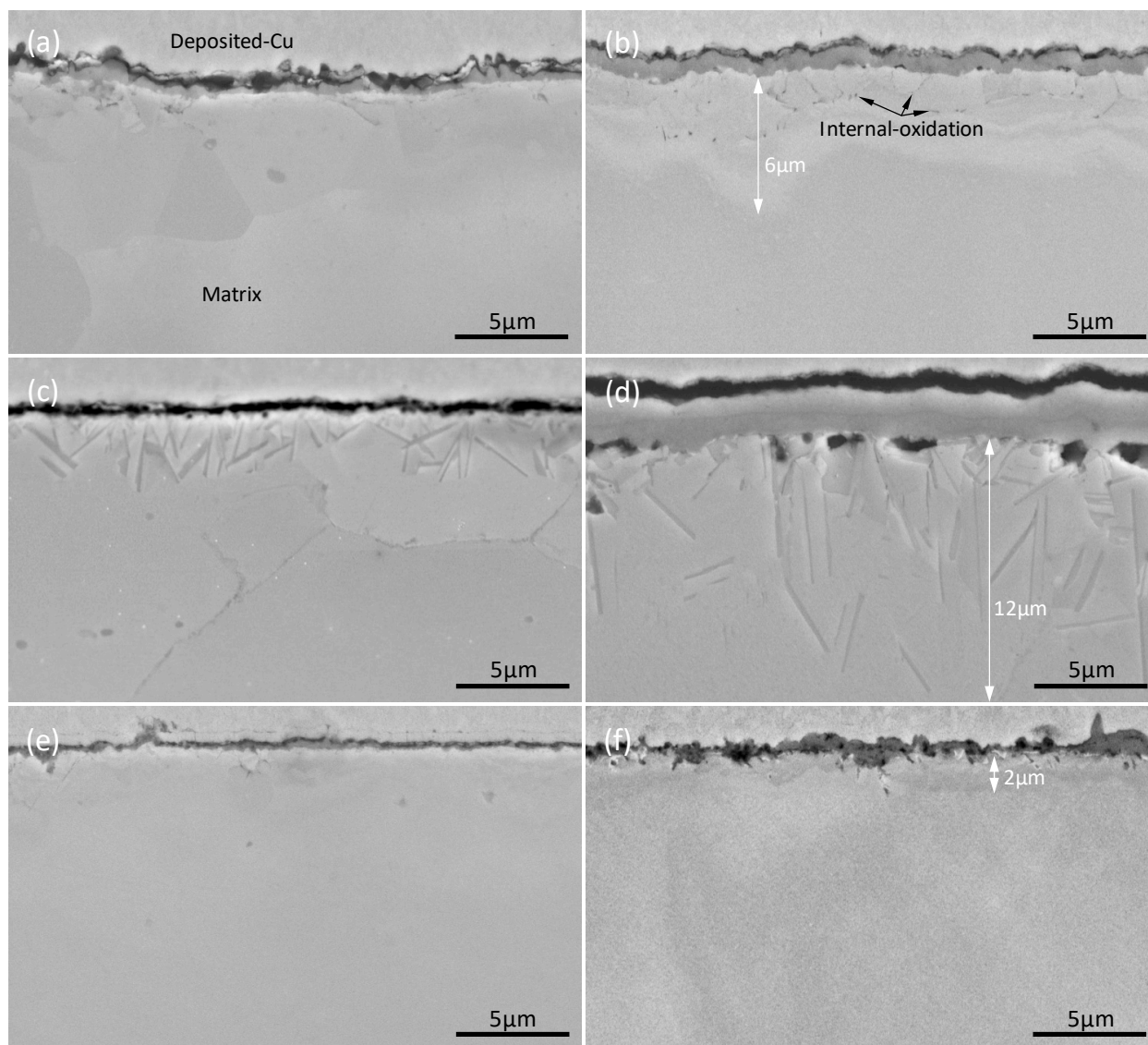


**Figure 2. Cross-sectional SEIs of the oxide scales formed on alloys (a-b) 690, (c-d) 725, and (e-f) X-750 exposed at (a, c, e) 600 and (b, d, f) 650°C for 5,000 h.**

Cross-sectional EDS line scans were conducted on the 650°C-5,000h-exposed samples, which are plotted in Figure 3, with the copper and oxygen denoted in open circles connected by dashed lines and the inherent primary alloying elements denoted in filled circles connected by solid lines. EDS line scans were not conducted on the 600°C-exposed samples because it was believed that the 600°C-exposed samples have similar elemental depth profiles as the 650°C-exposed samples, except for their much thinner scale and oxidation-influenced layer. The oxide scales are primarily enriched with Cr. Minor Ti enrichment was observed in the scales on alloys 725 and X-750 because of their high Ti content. Additionally, Ni-enriched oxide surface was observed on alloy 725. Beneath the scales, an oxidation-influenced layer showed noticeable Ni and minor/negligible Fe enrichment, together with noticeable Cr depletion. Minor Mo enrichment was also detected in the oxidation-influence layer of alloy 725 because of its high Mo content. Assuming 50% Cu as the scale surface, the overall oxidation-influenced thickness, including the scale, on alloys 690, 725, and X-750 exposed at 650°C for 5,000 h were measured to be ~5.6, ~9.7, and ~2.0 µm,

respectively, from the EDS line scan profiles, which are approximately consistent with the image-contrast-suggested thickness as shown in Figure 2b, d, f.

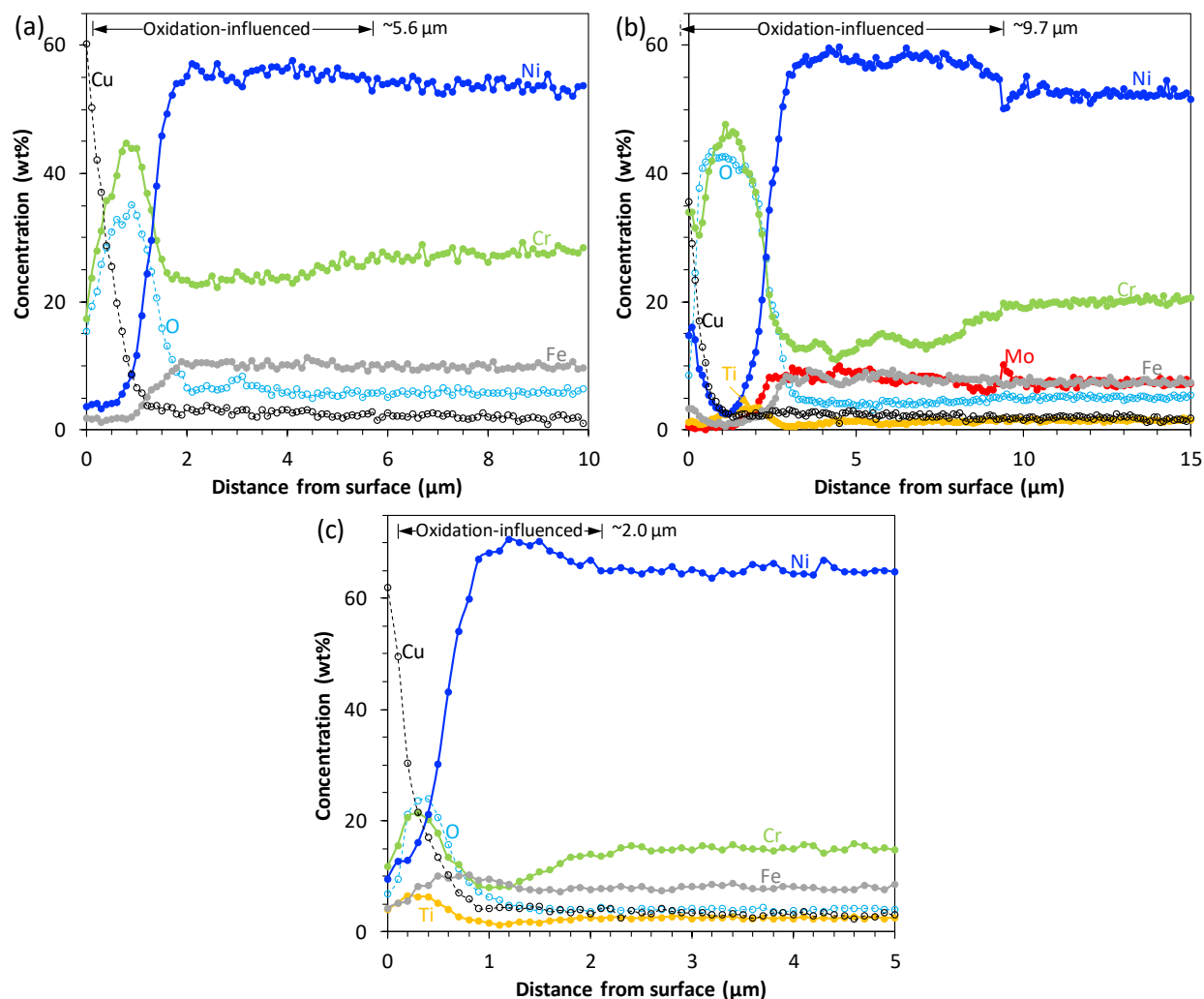


**Figure 3.** EDS line scan profiles across the scales on alloys (a) 690, (b) 725, and (c) X-750 exposed at 650°C for 5,000 h.

### 3.3 TEM AND EDS RESULTS

#### 3.3.1 Alloy 690

The TEM characterized microstructures of the 5000-h-exposed alloy 690 samples are shown in Figure 4 and Figure 5 for the 600 and 650°C exposures, respectively. The bright-field STEM images in Figure 4a and Figure 5a display scale in light gray on the right side, protected by a FIB-deposited Pt-layer. The 650°C-exposed sample has a noticeably thicker scale with an average thickness of 0.94  $\mu\text{m}$  in contrast to 0.30  $\mu\text{m}$  for the scale on the 600°C-exposed sample. The EDS maps in Figure 4b-c for the scale at (b) and (c) on the 600°C-exposed sample reveal discrete Ti- and Mn-rich oxides at outmost of the scale, followed by the dominant Cr-rich oxide and a thin Al-rich layer at the scale-matrix interface. Some globular particles in sub-micrometers appeared either at grain boundaries or within grains beneath the scale, as shown in Figure

4a at (d), which were characterized primarily containing Cr as shown by the EDS map in Figure 4d. Additionally, ultrafine Ni<sub>3</sub>Ti-type precipitates were observed in the 600°C-exposed sample as shown in the SAED pattern and its corresponding dark-field TEM image in Figure 4e-e'. The ultrafine Ni<sub>3</sub>Ti-type precipitates, having a size <5 nm dispersed in the matrix, excited additional reflections coherent with the face-centered cubic (fcc) matrix with an orientation relationship of  $[\bar{5}91]_{Ni_3Ti} \parallel [\bar{1}2\bar{1}]_{fcc}$ . The lattice parameter ratio of  $c/a$  was determined to be 1.677, close to the 1.631 of Ni<sub>3</sub>Ti-hP16 [19].

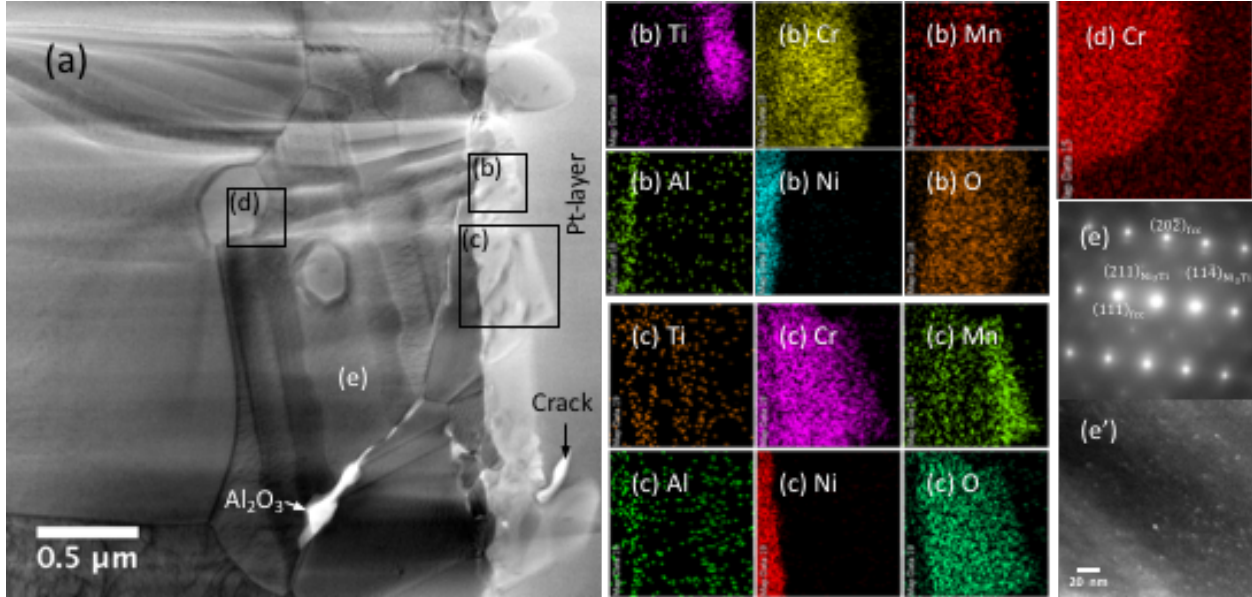


**Figure 4. (a) Bright-field STEM image of the 600°C-5000h-exposed alloy 690 and its (b-d) selected area EDS maps and (e) SAED pattern and corresponding (e') dark-field TEM image.**

Some discrete white features were observed beneath the scale, penetrating into matrix following grain boundaries as shown in Figure 4a and Figure 5a. Examples of selected area EDS map and SAED are shown in Figure 5b-c for the white features, which were characterized as Al-rich nature with a Al<sub>2</sub>O<sub>3</sub> diffraction pattern in the  $[\bar{7}32]$  zone axis. Compared to Figure 4e of the 600°C-exposed sample, the ultrafine precipitates were not observed in the 650°C-exposed sample as shown in Figure 5b having reflections only from matrix in the  $\langle 112 \rangle$  zone axis.

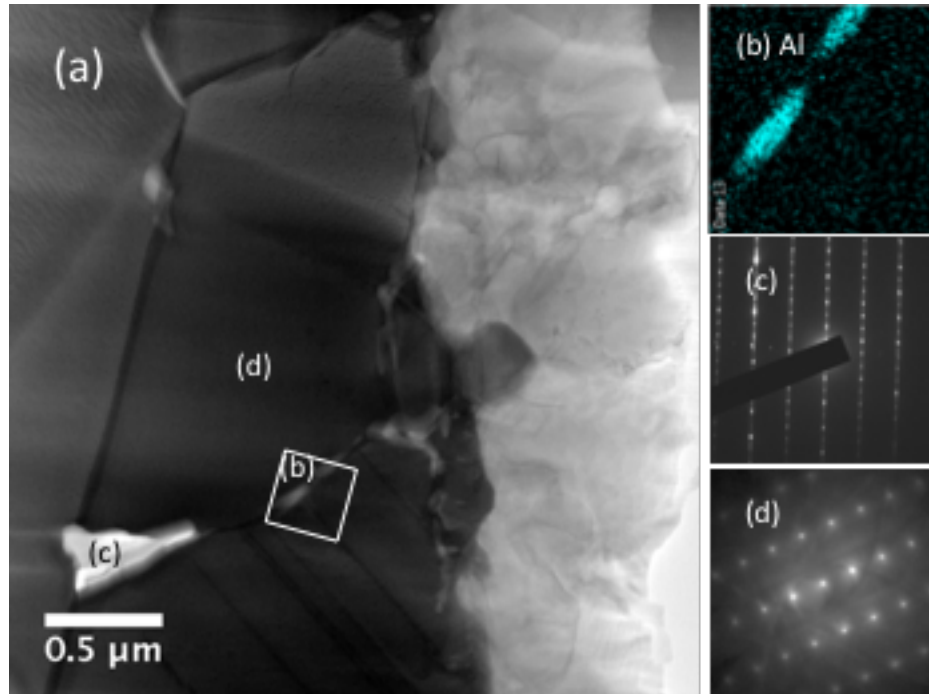


**Figure 5. (a) Bright-field STEM image of the 650°C-5000h-exposed alloy 690 and its (b) selected area EDS map and (c-d) SAED patterns.**

### 3.3.2 Alloy 725

The TEM/EDS characterization results of alloy 725 samples exposed to steam at 600 and 650°C for 5000 h are shown in Figure 6 and Figure 7, respectively, together with representative EDS spectra of the oxide and alloy phases in Figure 8. The 600°C-exposed sample in Figure 6a shows a thin scale (0.18 μm) on right side, in contrast to the thick scale (2.22 μm) on the 650°C-exposed sample in Figure 7a. The SAED patterns in Figure 6b-g at the locations from Figure 6a, coupled with EDS spectra as shown in Figure 8, was employed to identify the oxide and alloy phases. Oxide phases of Cr<sub>2</sub>O<sub>3</sub> in [001] (Figure 6b), Ti<sub>2</sub>O<sub>3</sub> in  $[\bar{1}11]$  (Figure 6c), and TiO<sub>2</sub> in [001] (Figure 6d), and alloy phases of μ (Mo/Ni/Si-rich) in  $[\bar{4}\bar{2}1]$  (Figure 6e), (Mo,Nb)Ni<sub>3</sub> in [001] (Figure 6f), and fcc matrix in [112] (Figure 6g) zone axes were identified, with their sampled locations schematically shown in Figure 6a. The scale was primarily composed of continuous Cr<sub>2</sub>O<sub>3</sub>, together with few discrete TiO<sub>2</sub> at surface and Ti<sub>2</sub>O<sub>3</sub> penetrating into matrix at some boundaries. The results from Figure 6a and associated phase characterization indicate that μ phase is big particles in sub-micrometers in an irregular shape, while (Mo,Nb)Ni<sub>3</sub> is lath-like particles corresponding to that revealed under SEM in Figure 2c-d. The SAED pattern of fcc in a [112] zone axis of Figure 6g, taken from the grain beneath the scale in Figure 6a, shows secondary reflections, which are believed to be excited from Ni<sub>3</sub>Ti-hP16 because it has the same zone axis family and secondary reflections as Figure 4e of alloy 690. However, the SAED pattern of fcc in a [011] zone axis in Figure 6h, taken from a grain far from the scale, exhibits secondary reflections as an ordered phase, which matches Ni<sub>3</sub>Ti-cP4 in a [011] zone axis with a deduced lattice parameter of  $a = 0.362$  nm assuming a lattice parameter of 0.357 nm for the fcc matrix. The dark-field TEM image in Figure 6i, using the  $(\bar{1}00)$  reflection enclosed in a dashed-line circle in Figure 6h, indicates that Ni<sub>3</sub>Ti-cP4 is dispersed in matrix in an elongated shape with lengths  $\sim 70$  nm.

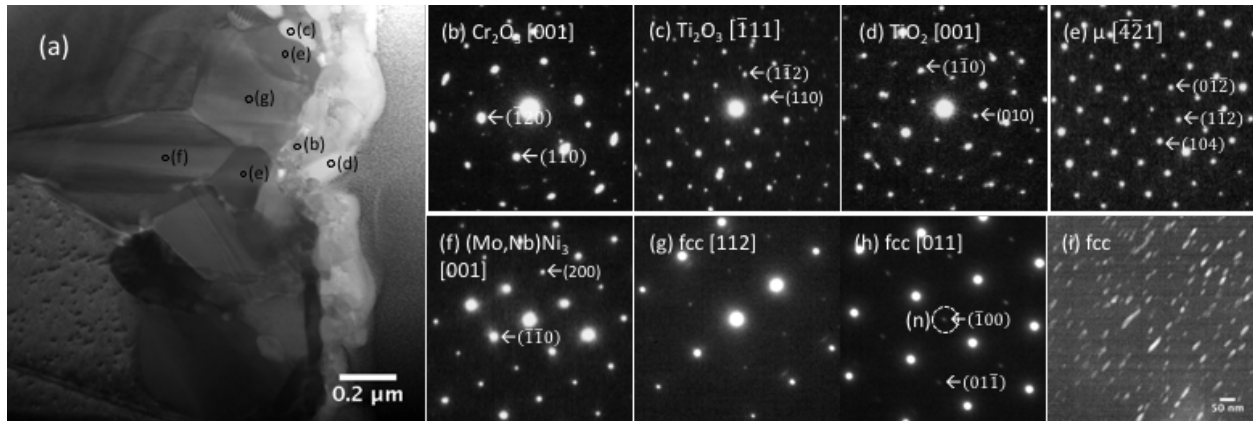


**Figure 6. (a) Bright-field STEM image of the 600°C-5000h-exposed alloy 725 and its (b-g) SAED patterns taken from the locations marked on (a), together with (h) SAED pattern from a grain far from the scale and its corresponding (i) dark-field TEM image.**

A pore is shown in the scale on the 650°C-exposed sample (Figure 7a), which was occasionally observed in the scale during FIB preparations. Figure 7b shows a high-angle annular dark-field (HAADF) image, taken from the white-line-outlined square region in Figure 7a, which reveals some dark features as Al-rich oxide. The EDS spectrum in Figure 8a indicates that the Al-rich oxide contains a high-intensity carbon peak, which may imply a complex form of Al-O-C compound. The limited size of the Al-rich features prevented them from SAED analysis. A few dark-gray features were also observed and identified as Cr<sub>2</sub>O<sub>3</sub> by EDS. Alloy phases such as  $\mu$  and (Mo,Nb)Ni<sub>3</sub> located at (e) and (f) in Figure 7b, respectively, were identified as that in the 600°C-exposed sample. The phase components in the scale were analyzed by SAED using a large aperture schematically shown in the Figure 7c with a white-line-outlined circle, which is shown in Figure 7c. Indexing of the diffraction ring pattern was assisted by CrysTBox [20] with excellent fitting confidence. Other than (Mo,Nb)Ni<sub>3</sub> that might have been captured from the adjacent particles, the scale was characterized to be a mixture of Ti<sub>2</sub>O<sub>3</sub>, TiO<sub>2</sub>, and NiCr<sub>2</sub>O<sub>4</sub>. The presence of Ni-rich oxide is consistent with the characterized Ni enrichment at surface as shown in Figure 3b.

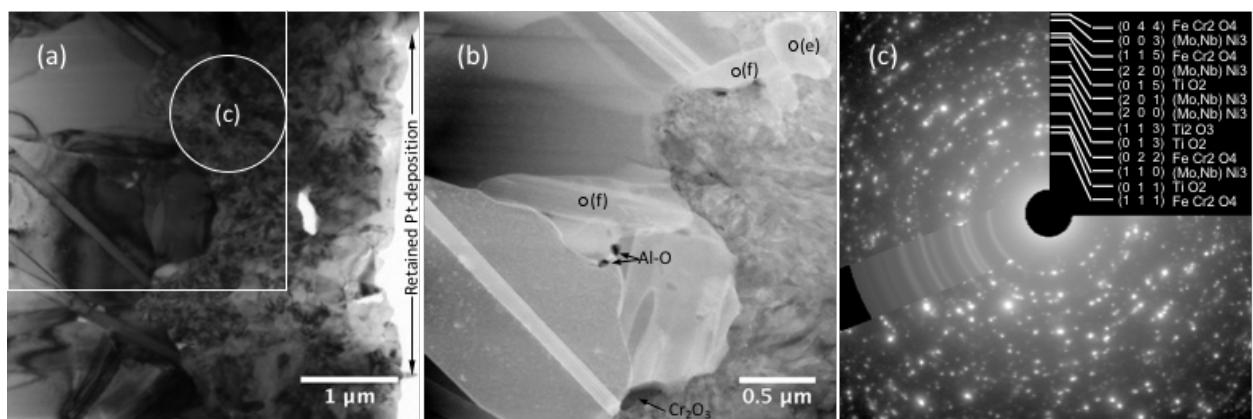


**Figure 7. (a) Bright-field STEM image of the 650°C-5000h-exposed alloy 725 and its corresponding (b) HAADF image and (c) SAED pattern from the locations schematically shown in (a).**

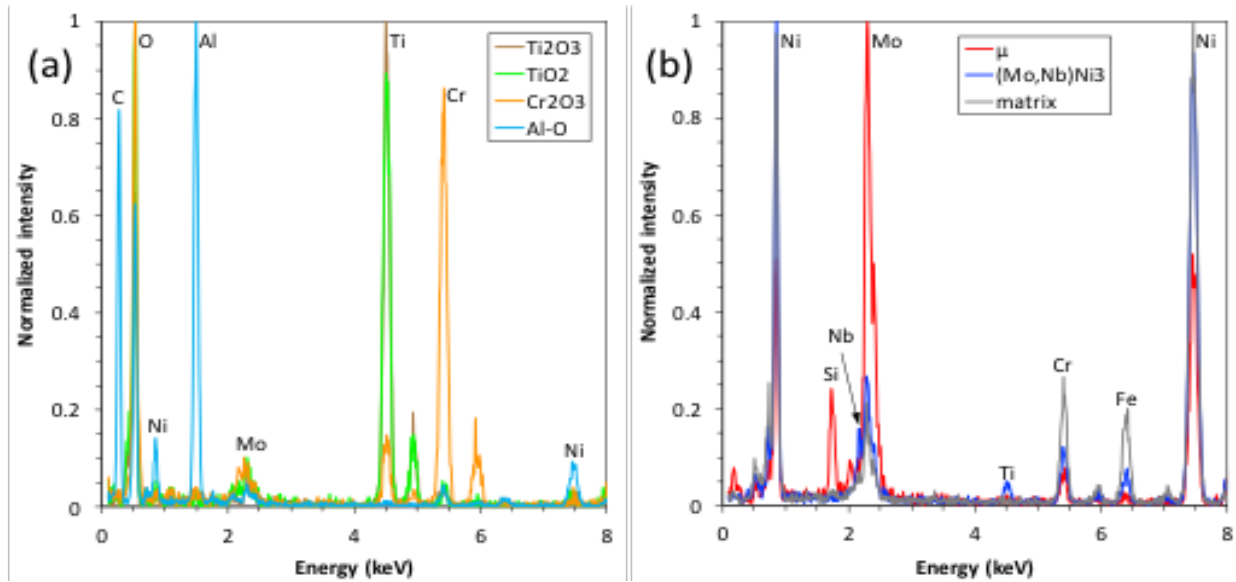


Figure 8. EDS spectra of (a) oxides and (b) alloy phases in alloy 725 exposed at 600 and 650°C for 5,000 h.

### 3.3.3 Alloy X-750

The TEM characterized microstructures of alloy X-750 exposed at 600 and 650°C for 5000 h are shown in Figure 9 and Figure 10, respectively. The bright-field STEM image in Figure 9a shows a thin scale (~0.12 μm) on the 600°C-exposed sample. One of the three internal oxidation features within the black-line-outlined square in Figure 9a was analyzed by EDS mapping with the primary elemental maps shown in Figure 9b. The internal oxidation is primarily Al/Ti-rich oxide and the scale is primarily composed of continuous Cr-rich oxide adjacent to the metal matrix and Ti-rich oxide at the outer scale. Figure 9c exhibits a diffraction ring pattern taken from the scale schematically within the black-line-outlined circle in Figure 9a. Indexing of the ring pattern yielded a mixture of Cr<sub>2</sub>O<sub>3</sub>, Ti<sub>2</sub>O<sub>3</sub>, TiO<sub>2</sub>, and FeCr<sub>2</sub>O<sub>4</sub> for the scale.

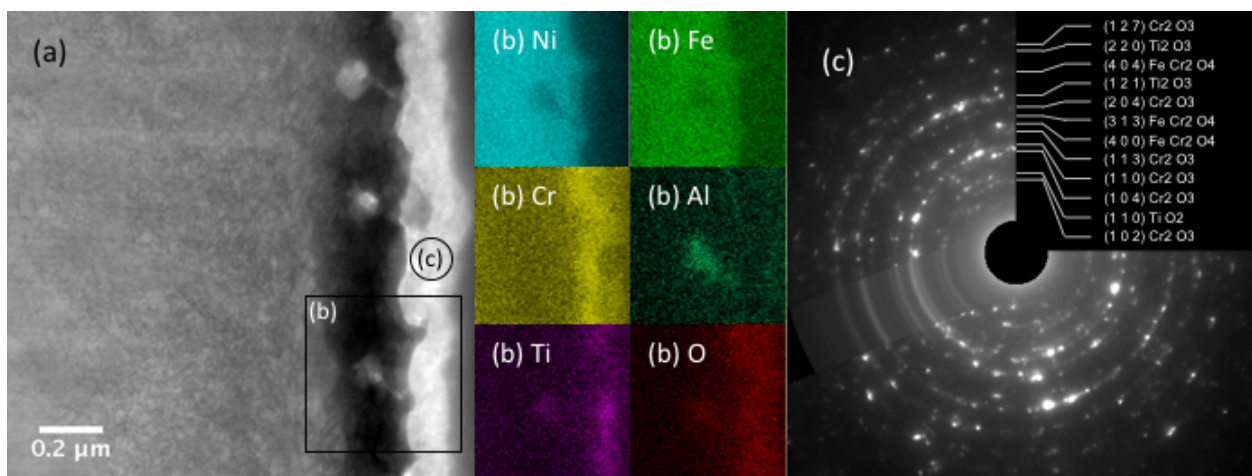
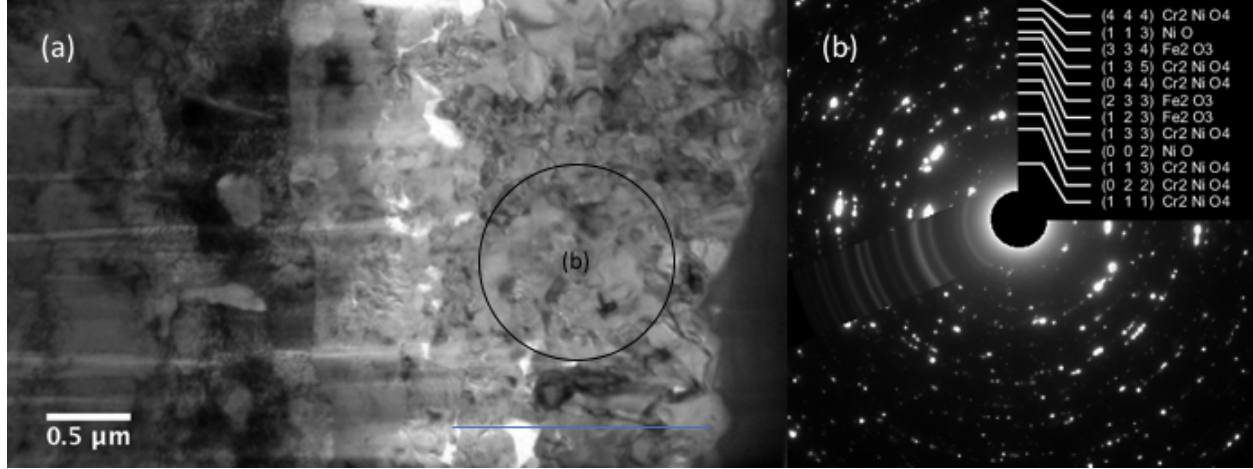


Figure 9. (a) Bright-field STEM image of 600C-5000h-exposed alloy X-750 and its corresponding (b) selected area EDS maps and (c) SAED pattern.

In comparison, the 650°C-exposed sample had a noticeably thicker scale (~1.52 μm) as shown by the bright-field TEM image in Figure 10a. A large-aperture produced SAED ring pattern in Figure 10b, taken from the region within the black-line-outlined circle in Figure 10a, indicates that the scale is primarily composed of a mixture oxide of NiCr<sub>2</sub>O<sub>4</sub>, Fe<sub>2</sub>O<sub>3</sub>, and NiO.



**Figure 10.** (a) Bright-field TEM image of 650°C-5000h-exposed alloy X-750 and its corresponding (b) SAED pattern.

### 3.4 DISCUSSION

#### 3.4.1 Computational Alloy Thermodynamics

Computational thermodynamics was employed to calculate the oxide stability of the alloy-oxygen systems using the JMatPro Ni-alloy database. Figure 11 plots the calculated phase amount in mole as a function of oxygen partial pressure for alloys (a) 690, (b) 725, and (c) X-750, together with (d) the calculated composition of M<sub>2</sub>O<sub>3</sub> as a function of oxygen partial pressure for the three alloys, exposed at 600°C. The 650°C condition had about the same layout of the phases and constituent elements of each phase as the 600°C condition, except for slight changes in the relative amounts of the phases and small moves of the layout to higher oxygen partial pressures (to right). The calculations indicate a dual-layer oxide structure on the three alloys. The outer layer is composed of NiO, AB<sub>2</sub>O<sub>4</sub>, and M<sub>2</sub>O<sub>3</sub>, together with some MoNb and (Mo,Nb)Ni<sub>3</sub> on alloy 725 (Figure 11b) and some Fe<sub>3</sub>O<sub>4</sub> and Ni<sub>3</sub>Nb on alloy X-750 (Figure 11c), according to the 10 ppb oxygen content in the steam that is approximately marked on the x-axis of Figure 11a-c. The inner layer is fcc metal mixed with M<sub>2</sub>O<sub>3</sub> and AB<sub>2</sub>O<sub>4</sub>, together with some Al<sub>2</sub>O<sub>3</sub> at the lowest oxygen partial pressures for the oxides on alloys 690 (Figure 11a) and X-750 (Figure 11c). Figure 11d suggests that M<sub>2</sub>O<sub>3</sub> has a varied composition from low to high oxygen partial pressure as Ti<sub>2</sub>O<sub>3</sub> → (Cr,Ti)<sub>2</sub>O<sub>3</sub> → (Ti,Cr,Fe)<sub>2</sub>O<sub>3</sub> → (Fe,Cr,Ti)<sub>2</sub>O<sub>3</sub>, where the elements in the parentheses are in a descending order in terms of concentration. The composition change of AB<sub>2</sub>O<sub>4</sub> as a function of oxygen partial pressure (not shown here) is relatively simpler, which changes from FeCr<sub>2</sub>O<sub>4</sub> in the inner layer to NiCr<sub>2</sub>O<sub>4</sub> in the outer layer. The high Al content (0.72 wt%) in alloy X-750 leads to some Cr being substituted by Al as Fe(Cr,Al)<sub>2</sub>O<sub>4</sub> and Ni(Cr,Al)<sub>2</sub>O<sub>4</sub>. The moderate Al content (0.23 wt%) in alloy 690 yielded negligible effect on the AB<sub>2</sub>O<sub>4</sub> composition.

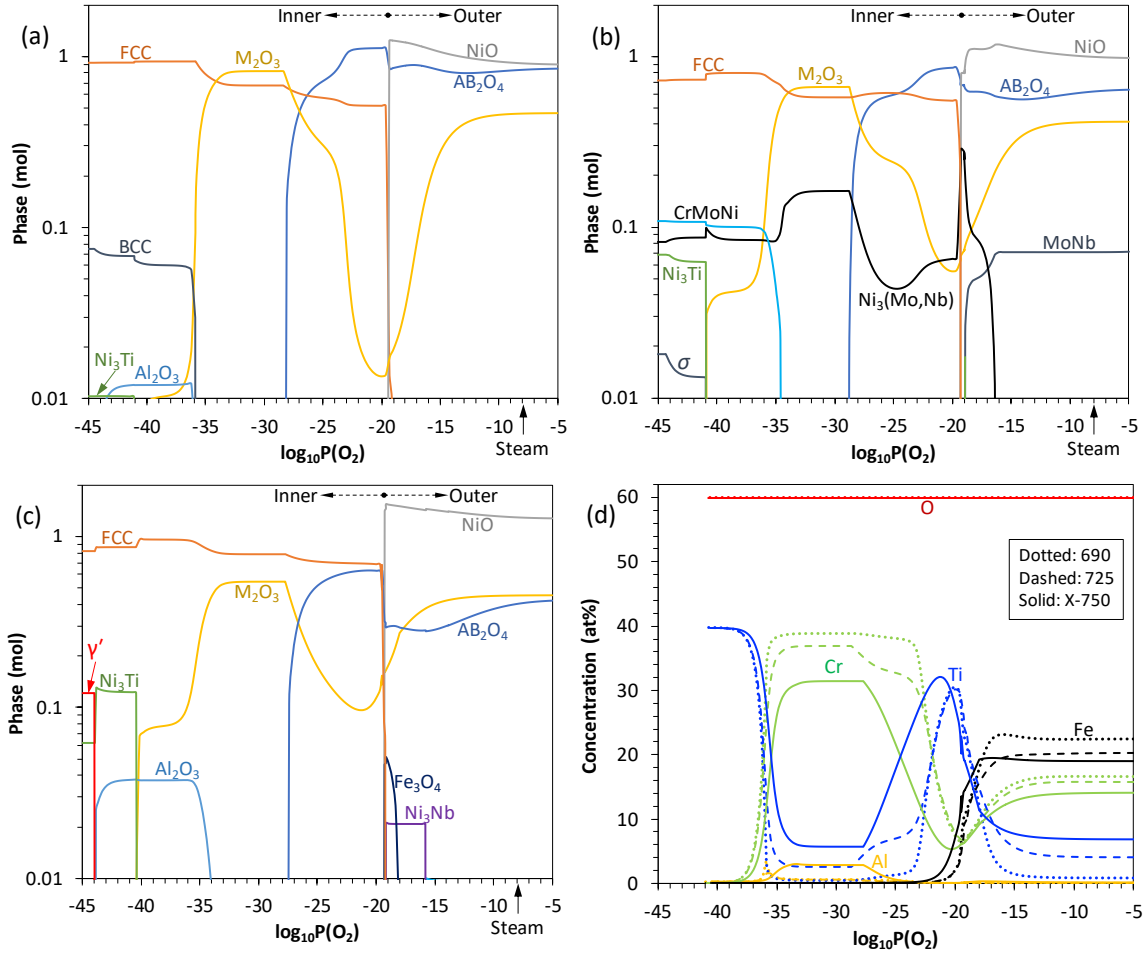


**Figure 11. Computational thermodynamics calculated oxygen-partial-pressure-dependent phase content for oxidation of 1 mole alloys (a) 690, (b) 725 and (c) X-750, together with the composition variation of  $M_2O_3$  at  $600^\circ\text{C}$ .**

According to the TEM characterization results, the characterized oxide and alloy phases for the three alloys exposed at 600 and  $650^\circ\text{C}$  for 5,000 h are summarized in Table 3. The experimental results are approximately consistent with the calculated results in Figure 11, in terms of the presence of  $M_2O_3$ . However, the calculation predicted  $AB_2O_4$  in the outer scale was only observed on alloys X-750 and 725 at  $650^\circ\text{C}$ . The predicted NiO in the outer scale was only observed on alloy X-750 at  $650^\circ\text{C}$ . The results imply that the outer scale was mostly exfoliated during the steam exposure and/or the “cyclic” cooling down for weighing, which favored the outer  $Ti_2O_3$  becoming  $TiO_2$  by the elevated oxygen partial pressure. The characterized alloy phases agree well with the thermodynamic calculations. The Cr-rich globular particles in alloy 690 corresponds to the calculated body-centered cubic (bcc) phase. Although dispersed  $Ni_3Ti$ -hP14 was observed in the fcc matrix of alloy 690 exposed at  $600^\circ\text{C}$ , this phase was not detected in the alloy exposed at  $650^\circ\text{C}$ . Comparing to the calculation of alloy 690 with 0.0104 mole at  $600^\circ\text{C}$  and 0.0073 mole at  $650^\circ\text{C}$  for  $Ni_3Ti$ , it implies that the undetected  $Ni_3Ti$  at  $650^\circ\text{C}$  was likely attributable to the amount of the phase lower than the TEM detection limit. Other than  $Ni_3Ti$ -hP14 in fcc matrix beneath scale, a metastable state of  $Ni_3Ti$ -cP4 was observed in the matrix far from the scale on alloy 725. Fig. 3b indicated composition changes beneath scale, e.g., Ni and Mo enrichment and Cr depletion, on alloy 725. The effect of composition variance on the stability of  $Ni_3Ti$  requires more detailed thermodynamics evaluation to

understand the evolution of the phase. Alloy phases  $\mu$  and  $(\text{Mo,Nb})\text{Ni}_3$  were characterized in alloy 725, but Cr-rich bcc phase was not observed, which might be attributable to the limited amount ( $<0.02$  mole) of the bcc phase compared to  $\mu$  and  $(\text{Mo,Nb})\text{Ni}_3$  with amounts  $\sim 0.1$  mole. The scattered sub-micrometer particles of the bcc phase were difficult to locate under TEM compared to the dispersed  $\text{Ni}_3\text{Ti}$  despite its less amount (e.g., 0.0104 mole in Figure 11a). Similarly, the other minor phases such as  $\text{Fe}_3\text{O}_4$  and  $\text{Ni}_3\text{Nb}$  predicted on alloy X-750 were not able to be observed.

**Table 3. TEM characterized oxide and alloys phases for alloys 690, 725, and X-750 exposed at 600 and 650°C for 5,000 h**

Alloy	Oxide					Alloy phase			
	$\text{Al}_2\text{O}_3$	$\text{Cr}_2\text{O}_3$	$\text{Ti}_2\text{O}_3$ or $\text{TiO}_2$	$\text{AB}_2\text{O}_4$	$\text{NiO}$	$\text{Ni}_3\text{Ti}$	Cr	$\mu$	$(\text{Mo,Nb})\text{Ni}_3$
690	present	present	either	absent	absent	hP14 (not at 650°C)	present	inapplicable	inapplicable
725	present (with carbon)	present	both	present (not at 600°C)	absent	hP14 and cP4	absent	present	present
X-750	present	present	both	present	present (not at 600°C)	Not characterized	inapplicable	inapplicable	inapplicable

### 3.4.2 Exfoliation of Oxide Scale

The relationships between mass change, scale thickness (both from SEM and TEM results), and calculated oxide phase fraction in outer scale for alloys 690, 725, and X-750 exposed at 600 and 650°C for 5,000 h are summarized in Figure 12. The 600°C results in Figure 12a indicate that the scale thickness characterized under TEM was generally thinner than that under SEM, which is contrary to the 650°C results in Figure 12b. The TEM-characterized thicknesses were generally within the standard deviation ranges of the SEM-characterized thickness, except for alloy 725 at 600°C and alloy X-750 at 650°C. However, the TEM-characterized thicknesses on alloy 725 at 600°C and alloy X-750 at 650°C were still within the minimum or maximum thickness characterized by SEM. Basically, thicker scales are correlated with either greater mass losses at 600°C or greater mass gains at 650°C. The thicker scales with greater mass losses at 600°C, e.g., alloys 690 and 725, may suggest greater metal losses that exceeded the scales-induced mass gains. The phase fraction in Figure 12 is average values of the oxide phases in outer scale below 10 ppb oxygen partial pressure from Figure 11a-c. Figure 12a indicates greater mass losses with increased  $\text{NiCr}_2\text{O}_4$  and reduced  $\text{NiO}$  and  $\text{M}_2\text{O}_3$  at 600°C. On the other hand, greater mass gains are associated with reduced  $\text{NiO}$  and  $\text{M}_2\text{O}_3$ , but varied  $\text{NiCr}_2\text{O}_4$  at 650°C as shown in Figure 12b.

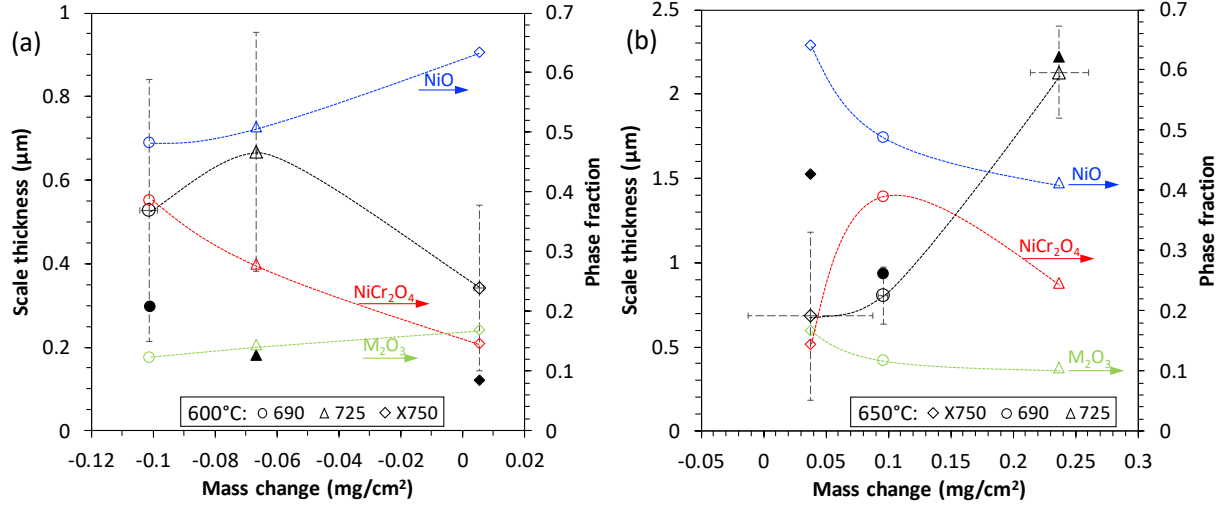


**Figure 12. Relationship between mass change, scale thickness, and calculated oxide phase fraction in outer scale for alloys 690 (circles), 725 (triangles), X-750 (diamonds) exposed at (a) 600°C and (b) 650°C. The open and filled black symbols denote the thickness data obtained from SEM and TEM characterization, respectively.**

Thermal expansion incompatibility is one of the key factors causing scale exfoliations. Figure 13 plots the temperature-dependent thermal expansion coefficients of a variety types of oxides [21,22], together with that of the three alloys from vendors' alloy specifications. The thermal expansion coefficients of the oxides are generally either comparable to or lower than (but with similar changing slopes) that of the alloys, except for  $Ti_2O_3$  and  $NiCr_2O_4$ .  $Ti_2O_3$  adjacent to metals as suggested in Figure 11d was barely observed, while  $(Ti,Cr,Fe)_2O_3$  at the inner-outer scale interface as suggested in Figure 11d was identified as shown in Figure 10a-c. The partial substitution of Cr and Fe for Ti in  $Ti_2O_3$  may reduce the thermal expansion discrepancy between the oxide and metals as suggested by the excellent match or lower thermal expansion coefficients of  $Fe_2O_3$  and  $Cr_2O_3$  compared with that of the metals. However, significant thermal expansion discrepancy between  $NiCr_2O_4$  and metals (and other oxides) could not be alleviated, resulting in outer scale exfoliations. Consequently,  $NiCr_2O_4$  (the outer scale) was only observed on alloys 725 only at 650°C and X-750 at both temperatures, which correlate with their low  $NiCr_2O_4$  fractions ( $<0.25$ ). Additionally, the partial Al-substitution in  $Ni(Cr,Al)_2O_4$  on alloy X-750 because of its high Al content, suggested by the thermodynamic calculation, would alleviate the thermal expansion discrepancy between  $Ni(Cr,Al)_2O_4$  and metal according to Ref. [23], which favored the integrity of the scale on alloy X-750.

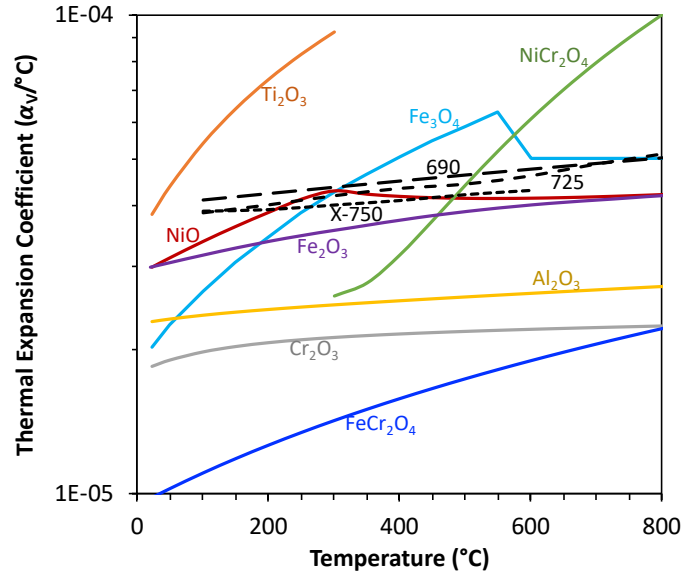


**Figure 13. Temperature-dependent thermal expansion coefficients of oxide phases and matrix alloys 690, 725, and X-750.**

Figure 1 indicates general mass losses at 600°C but mass gains at 650°C. Kinetics is believed to be a primary factor resulting in the contrast. As shown in Figure 14 with tracer diffusion coefficient ( $D$ ) in Ni as a function of temperature [ $1000/T$  (1/K)] [24], the diffusion coefficient of Cr follows a two-section linear relationship, having a transition point at 600°C, above which the diffusion coefficient increases at a noticeably higher rate. In contrast, the diffusion coefficients of Fe and Ni have a linear relationship with  $1/T$  in the same temperature range. Million, et al., found that the same relation of self-diffusion coefficients,  $D_{Ni}^* : D_{Fe}^* : D_{Cr}^* = 1 : 1.2 : 2$ , was maintained within a large range of composition in Fe-(16–87)Ni-(0–32)Cr alloys with fcc lattice at 1013 – 1275°C [25]. Assuming the negligible composition effect on the ratios of the diffusion coefficients can be extended into lower temperatures despite the change in the ratios of the relation, the actual diffusion coefficients of the three primary elements in the alloys would not change the singular linear relationships for Fe and Ni and the two-section linear relationship for Cr as shown in Figure 14. The noticeably enhanced Cr diffusivity at 650°C favored stable scale development compared to the scales at 600°C.

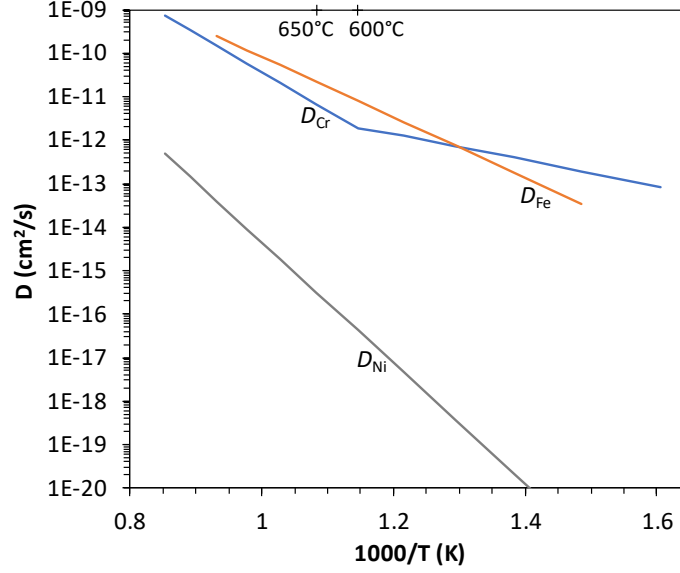


Figure 14. Tracer diffusion coefficients of Cr, Fe, and Ni in Ni [24].

### 3.4.3 Metal Thickness Loss by the Steam Exposures

Assuming uniform oxidation at the edge, the same as that at the large surfaces of the tested coupons, and letting  $A$  as the large surface area and  $t_0$  (from the black dashed line as schematically shown in Figure 15a) as the initial thickness of the tested coupons,  $t_m$  as the final metal thickness (in black shade in Figure 15a) and  $t_s$  as the scale thickness (in green shade in Figure 15a) after the steam exposures, the measured weight after the steam exposure  $W_1 \approx W_s + W_0 \times t_m/t_0$ , where  $W_s$  and  $W_0$  are the weight of the scale and the initial coupon, respectively. With the density of the scale  $\rho_s = \frac{W_s}{2kAt_s}$  and nominal density of the scale  $\rho'_s = \frac{W_1 - W_0}{2kAt_s}$ , the scale density difference

$$\rho_s - \rho'_s = \frac{W_0 \left(1 - \frac{t_m}{t_0}\right)}{2kAt_s} = \frac{W_0}{At_0} \frac{\Delta t}{2kt_s} = \rho_0 \frac{\Delta t}{2kt_s},$$

where  $\rho_0$  is the initial metal density,  $\Delta t = t_0 - t_m$  as the thickness loss of the metal, and  $k = S/2A \approx 1.23$  as a ratio of the overall surface area ( $S$ ) over the two large surface areas of the test coupons. Therefore,

$$\Delta t = \frac{\rho_s - \rho'_s}{\rho_0} 2kt_s.$$

The microstructural characterization indicated that the scale was primarily composed of  $M_2O_3$ ,  $AB_2O_4$ , and  $TiO_2$ , with theoretical density in the range of 4.23 ( $TiO_2$ ) to 5.22  $g/cm^3$  ( $Cr_2O_3$ ). The effect of  $Al_2O_3$  (3.95  $g/cm^3$ ) on the overall scale density is negligible because of its limited amount. The  $\rho_s$  can be estimated to be  $\sim 5 g/cm^3$  according to the relative content of the oxide components. The  $\rho'_s$  of the 600°C-exposed samples can be deduced from Figure 12a as -1.92, -1.00, and 0.16  $g/cm^3$  and the 650°C-exposed samples from Figure 12b as 1.19, 1.11, and 0.55  $g/cm^3$  for the scales on alloys 690, 725, and X-750, respectively, using the SEM-characterized scale thicknesses. With the  $\rho_0$  of the alloys, i.e., 8.12, 8.31, and 8.14  $g/cm^3$  for alloys 690, 725, and X-750, respectively, and the  $t_s$  (SEM-characterized) from Figure 12, the  $\Delta t$  can be estimated to be 1.10, 1.18, 0.50  $\mu m$  at 600°C and 0.93, 2.45, and 0.92  $\mu m$  at 650°C for alloys 690, 725, and X-750, respectively, which are plotted in Figure 15b.

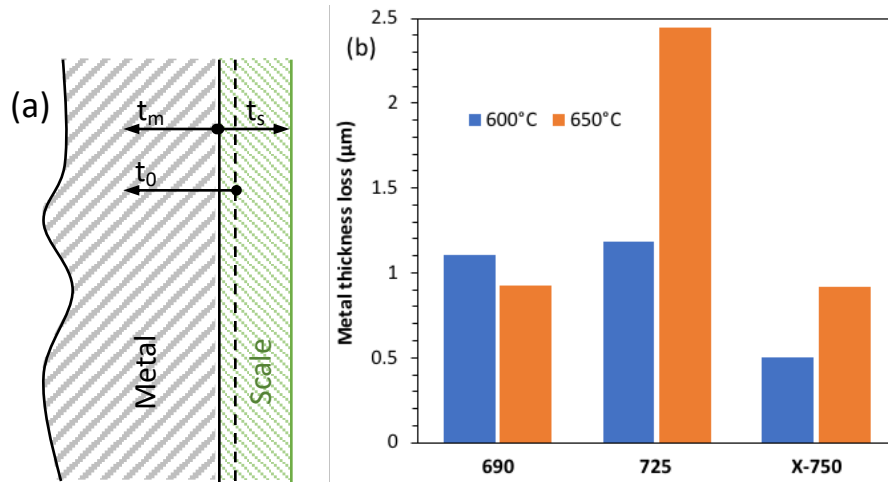


**Figure 15. (a) Thickness of the initial metal ( $t_0$ ) and the metal ( $t_m$ ) and scale ( $t_s$ ) after steam exposures; (b) Estimated metal thickness loss ( $\Delta t$ ) of alloys 690, 725, and X-750 exposed at 600 and 650°C for 5,000 h.**

#### 4. FRACTURE TOUGHNESS TESTED SAMPLES

Fracture toughness test was conducted on eight alloys, i.e., Grade 92, 14YWT, 316L, 310, 690, 718A, 725, and X-750, at room temperature, 250, 300, and 350°C [26,27]. Photos of the fracture toughness tested samples at room temperature and 300°C for ferritic alloys Grade 92 and 14YWT and austenitic stainless steels 316L and 310 are shown in Figure 16. The 300°C-tested 316L was not acceptable according to the relevant ASTM standard (e.g., ASTM E1820-13) for fracture toughness testing and thus the 250°C-tested 316L is displayed in Figure 16. Similarly, the photos of Ni-base superalloys 690, 718A, 725, and X-750 are shown in Figure 17. The left- and right-half sample exhibits the side-view and fractured surface, respectively, for each sample. The samples were heat-tinted to reveal the stable crack extension, beginning at the end of the flat fatigue precracked area (the “triangle” area on the right-half sample) and ending at the end of heat tint area.

To better understand the fracture toughness behavior of the variety of alloys, a few tasks will be purposed in near future. Based on the previously collected fracture toughness data, microstructural characterization using SEM and electron backscattered diffraction, and possibly TEM, will be conducted on select tested samples that exhibited high, moderate, and low fracture toughness to understand the influence of microstructures on different fracture toughness behavior. In the meantime, tensile tests for the same heat materials will be conducted to correlate tensile properties with the fracture toughness results.



**Figure 16. Photos of fracture toughness tested samples at room temperature and 300°C (or 250°C) for ferritic alloys Grade 92 (G92) and 14YWT and austenitic stainless steels 316L and 310.**

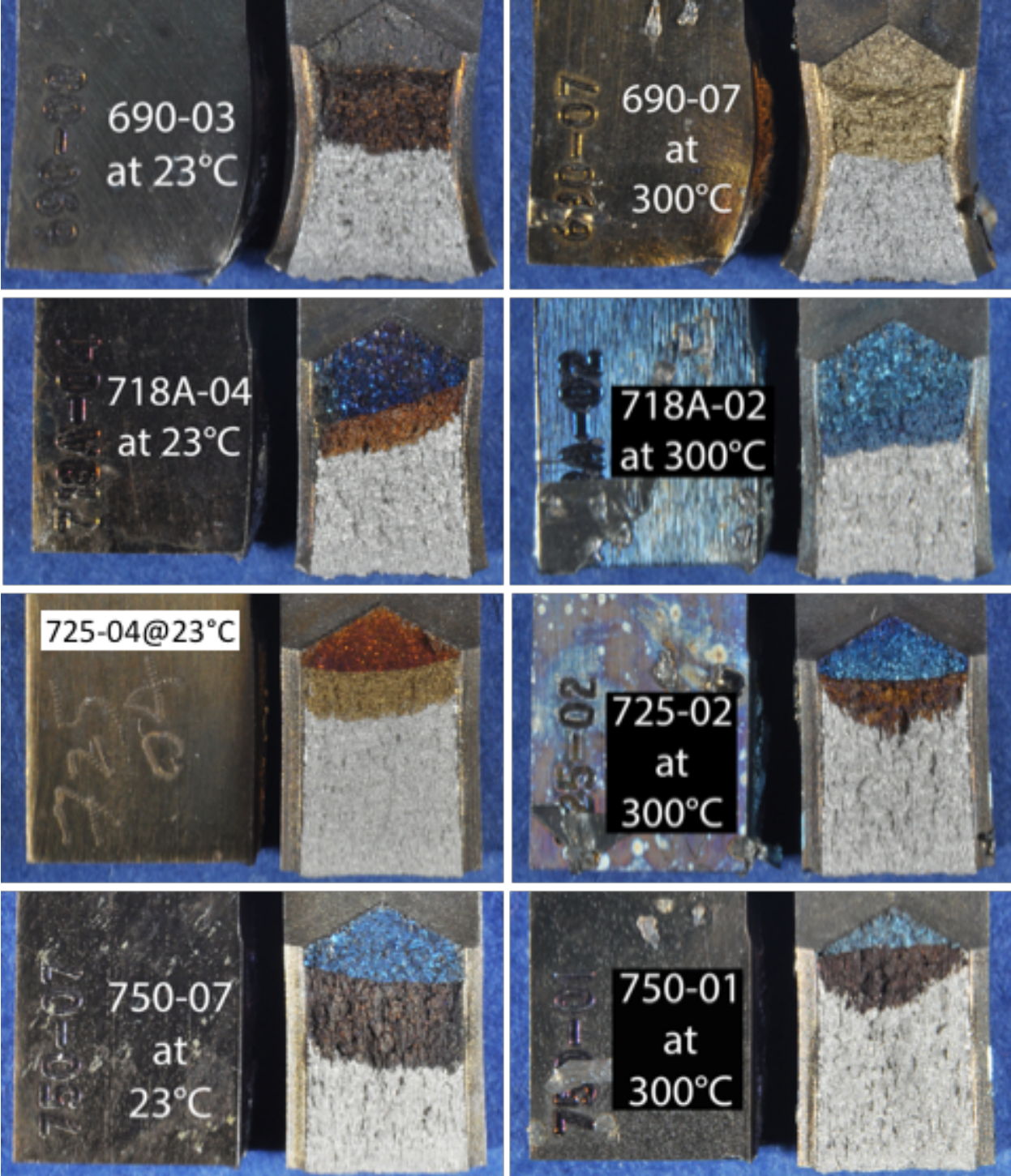


Figure 17. Photos of fracture toughness tested samples at room temperature and 300°C for Ni-base superalloys 690, 718A, 725, and X-750.

## 5. SUMMARY

Coupons of alloys 690, 725, and X-750 were exposed to 1 bar steam with ~10 ppb oxygen content at 600 and 650°C for up to 5,000 h. Mass changes of the coupons indicated general mass losses at 600°C but mass gains at 650°C. To understand the distinct behavior, microstructural characterization using SEM, TEM, and EDS was conducted on the samples exposed to 5,000 h at the two temperatures. Together with computation alloy thermodynamics and the nature of the oxides and the diffusivities of primary elements, quantitative metal loss behavior of the three alloys was identified.

SEM, TEM, and EDS characterization revealed significantly thicker scales at 650°C compared to that at 600°C, which were primarily composed of Cr<sub>2</sub>O<sub>3</sub>, Ti<sub>2</sub>O<sub>3</sub>, Al<sub>2</sub>O<sub>3</sub>, FeCr<sub>2</sub>O<sub>4</sub>, NiCr<sub>2</sub>O<sub>4</sub>, NiO, and TiO<sub>2</sub>. The results are generally consistent with thermodynamic calculations, except for TiO<sub>2</sub> that is believed to be formed by the outer-scale exfoliation raising the local oxygen partial pressure. The steam exposures resulted in an extensive oxidation-influenced layer beneath the scales, which favored the formation of additional precipitates such as (Mo,Nb)Ni<sub>3</sub> in alloy 725. Other phases such as Cr-rich bcc phase and Ni<sub>3</sub>Ti were observed beneath the scales as predicted by the thermodynamic calculations.

Analyzing the relationships between mass change, scale thickness, and the calculated oxide phase fraction indicates that high fraction of NiCr<sub>2</sub>O<sub>4</sub> is correlated with greater mass losses and scale instability because of the large thermal expansion discrepancy between this oxide and metal (and other oxides). The significantly increased diffusivity of Cr at 650°C favored the better scale development and integrity compared to that at 600°C, e.g., general mass gains vs. mass losses. The 5000-h exposures resulted in varied metal thickness losses. The estimation suggests that alloy X-750 had the least metal thickness loss (<1 μm), slightly less than alloy 690. Despite the metal loss of alloy 725 is only slightly more than that of alloy 690 at 600°C, the metal thickness loss of alloy 725 (~2.5 μm) is nearly three times of that of alloys 690 and X-750 at 650°C, which might be attributable to its high Mo content, tending to form volatile MoO<sub>3</sub> with elevated volatility at 650°C.

Photos of the fracture toughness tested samples of eight alloys are presented, which will be correlated with their fracture toughness results and planned tensile test results to select representative alloy samples for detailed microstructural characterization to reveal their microstructure and properties relationships.

## REFERENCES

- 
- [1] E.A. Kenik, J.T. Busby, Radiation-induced degradation of stainless steel light water reactor internals, *Mater. Sci. Eng. R* 73 (2012) 67–83.
  - [2] F.A. Garner, Radiation damage in austenitic steels, in: R.J.M. Konings, T.R. Allen, R.E. Stoller, S. Yamanaka, *Comprehensive Nuclear Materials*, Elsevier, The Netherlands, 2012.
  - [3] L. Tan, R.E. Stoller, K.G. Field, Y. Yang, H. Nam, D. Morgan, B.D. Wirth, M.N. Gussev, J.T. Busby, Microstructural evolution of type 304 and 316 stainless steels under neutron irradiation at LWR relevant conditions, *JOM* 68 (2016) 517–529.
  - [4] Critical Issues Report and Roadmap for the Advanced Radiation-Resistant Materials Program, EPRI, Palo Alto, CA and the U.S. Department of Energy, Washington, DC: 2012. 1026482.
  - [5] J.C.M. Farrar, *The alloy tree – A guide to low-alloy steels, stainless steels and nickel-base alloys*, Woodhead Publishing Limited, Cambridge, England, 2004.
  - [6] S.K. Mannan, S.J. Patel, J. Dong, X. Xie, Crack growth and high temperature thermal stability of Inconel alloy 725, in: D.G. Morris, S. Naka, P. Caron (Eds.), *Intermetallics and Superalloys, EUROMAT 99*, Vol. 10, Wiley-VCH Weinheim, Germany, 2000, p.15-21.
  - [7] G.D. Smith, B.A. Baker, *Mechanical Engineers' Handbook: Materials and Mechanical Design*, Vol. 1, Chapter 6 Nickel and Its Alloys, John Wiley & Sons, Inc., 2006, p.256–277.
  - [8] S.J. Zinkle, J.T. Busby, Structural materials for fission & fusion energy, *Mater. Today* 12 (2009) 12–19.
  - [9] W. Kuang, M. Song, P. Wang, G.S. Was, The oxidation of alloy 690 in simulated pressurized water reactor primary water, *Corros. Sci.* 126 (2017) 227–237.
  - [10] T. Moss, G. Cao, G.S. Was, Oxidation of alloy 600 and alloy 690: experimentally accelerated study in hydrogenated supercritical water, *Metall. Mater. Trans. A* 48 (2017) 1596–1612.
  - [11] X. Zhong, E.-H. Han, X. Wu, Corrosion behavior of alloy 690 in aerated supercritical water, *Corros. Sci.* 66 (2013) 369–379.
  - [12] X. Zhong, X. Wu, E.-H. Han, Characteristics of oxidation and oxygen penetration of alloy 690 in 600°C aerated supercritical water, *J. Mater. Sci. Tech.* 34 (2018) 561–569.
  - [13] S. Tuzi, K. Göransson, S.M.H. Rahman, S.G. Eriksson, F. Liu, M. Thuvander, K. Stiller, Oxide evolution on alloy X-750 in simulated BWR environment, *J. Nucl. Mater.* 482 (2016) 19–27.
  - [14] J. Chen, F. Linderg, L. Belova, B. Forssgren, K. Gott, J. Lejon, A. Jasiulevicius, High resolution electron microscopy study on oxide films formed on nickel-base alloys X-750, 182 and 82 in simulated high flow velocity BWR water conditions, in: J.T. Busby, G. Ilevbare, P.L. Andresen (Eds.), *15<sup>th</sup> International Conference on Environmental Degradation*, TMS (The Mineral, Metals & Materials Society), 2011, John Wiley & Sons, Inc., Hoboken, New Jersey, USA.
  - [15] Q. Zhang, R. Tang, C. Li, X. Luo, C. Long, K. Yin, Corrosion behavior of Ni-base alloys in supercritical water, *Nucl. Eng. Tech.* 41 (2009) 107–112.
  - [16] *Safety Aspects of Water Chemistry in Light Water Reactors*, IAEA-TECDOC-489, International Atomic Energy Agency, Vienna, 1988.
  - [17] M. Montgomery, A. Karlsson, Survey of oxidation in steamside conditions, *VGB Kraftwerkstechnik* 75 (2009) 235–240.
  - [18] Y. Ootoguro, M. Sakakibara, T. Saito, H. Ito, Y. Inoue, Oxidation behavior of austenitic heat-resisting steels in a high temperature and high pressure steam environment, *Trans. Iron Steel Inst. Jpn.* 28 (2008) 761–768.
  - [19] National Institute for Materials Science (NIMS) AtomWork <<http://crystdb.nims.go.jp/>> (Accessed: Aug. 13, 2018).
  - [20] M. Klinger, More features, more tools, more CrysTBox, *J. Appl. Cryst.* 50 (2017) 1226–1234.
  - [21] Y. Fei, Thermal Expansion, in: *Mineral Physics and Crystallography - A Handbook of Physical Constants*, AGU Reference Shelf 2, the American Geophysical Union, 1995.

- 
- [22] L.J. Eckert, R.C. Bradt, Thermal expansion of corundum structure  $Ti_2O_3$  and  $V_2O_3$ , *J. Appl. Phys.* 44 (1973) 3470.
- [23] I. Zaplatynsky, Thermal expansion of some nickel and cobalt Spinel and their solid solutions, NASA Technical Note, NASA TN D-6174, National Aeronautics and Space Administration, Washington, D.C., February 1971.
- [24] J. Askill, Tracer Diffusion Data for Metals, Alloys, and Simple Oxides, IRI/Plenum Data Corporation, New York, NY, 1970.
- [25] B. Million, J. Růžicková, J. Vřešťál, Diffusion in Fe–Ni–Cr alloys with f.c.c. lattice, *Mater. Sci. Eng.* 72 (1985) 85–100.
- [26] X. Chen, L. Tan, Fracture toughness evaluation of select advanced replacement alloys for LWR core internals, ORNL/TM-2017/377, August 25, 2017.
- [27] L. Tan, B.A. Pint, X. Chen, Toughness and high-temperature steam oxidation evaluations of advanced alloys for core internals, ORNL/TM-2016/371, September 16, 2016.